Decoupling of the softening processes during rapid tempering of a martensitic steel

Elliot Biro [a,b], Joseph R. McDermid [c,*], Samuel Vignier [a], Y. Norman Zhou [d]

[a] ArcelorMittal Global Research, 1390 Burlington Street, Box 2460, Hamilton, Ont., Canada L8N 3J5
[b] Deptartment of Materials Science and Engineering, McMaster University, 1280 Main Street West, Hamilton, Ont., Canada L8S 4L8
[c] McMaster Steel Research Centre, McMaster University, 1280 Main Street West, Hamilton, Ont., Canada L8S 4L8
[d] Deptartment of Mechanical and Mechatronics Engineering, University of Waterloo, 200 University Avenue West, Waterloo, Ont., Canada N2L 3G1

ARTICLE INFO

ABSTRACT

The increased adoption of martensite-containing advanced high strength steels, such as martensitic and dual-phase steels, into automotive applications has led to concerns among practitioners with respect to softening during rapid tempering cycles such as those experienced during laser welding. Past studies on rapid tempering have successfully modeled the rapid tempering process; however, the activation energies and softening rates calculated did not match the classic literature values associated with martensite tempering. The present study examined rapid tempering data for a martensitic steel and separated the softening process into two stages: carbide nucleation and carbide coarsening or growth. The activation energies calculated for each process were found to be consistent with classic literature values for diffusion controlled nucleation and growth of carbides during martensite tempering.

© 2014 Elsevier B.V. All rights reserved.

1. Introduction

Automotive manufacturers are widely required by legislation to improve vehicle fuel economy [1]. Among the solutions being pursued to realize this objective is structural component weight reduction by reducing steel sheet thickness. However, in order to meet structural requirements while reducing material thickness, automakers are replacing lower strength conventional steels with higher strength advanced high strength steel (AHSS) grades such as martensitic, dual-phase (DP) and transformation induced plasticity (TRIP) steels [2].

AHSS derive their high strengths from complex microstructures comprising mixtures of various volume fractions of martensite, ferrite, bainite and retained austenite [3,4]. Although all of these alloys exhibit an excellent strength–ductility balance, they contain phases that decompose at higher temperatures. In automotive assembly, this is observed in the tempered area of weld heat affected zones (HAZ), where martensite and (if present) retained austenite typically decompose during welding and the local hardness and ultimate tensile strength decrease [5,6]. This phenomenon, known as HAZ softening, was first observed in flash-butt wheel rim welding applications [7,8]. Since its initial

characterization, a number of authors have investigated HAZ softening. Some early workers concluded that HAZ softening was a strong function of the length of time the material temperature was elevated [9–11]. In these studies, HAZ softening was reduced by increasing the cooling rate after welding, thereby reducing the overall time the weldment was at an elevated temperature. Further work into this phenomenon has shown that HAZ softening is also related to material chemistry and initial microstructure. For example, the maximum HAZ softening possible in DP steels has been shown to be linearly dependant on martensite volume fraction [12] as the observed hardness decrease was due to martensite decomposition whereas no significant hardness changes were observed in the ferritic matrix [13]. Other authors have shown that HAZ softening kinetics are affected by alloy chemistry. For instance, increasing the martensite C content has been found to increase the softening rate [6]. Conversely, alloying with carbide forming elements (e.g. Cr, Mo) has been shown to slow softening by either retarding cementite precipitation or growth within the tempered martensite [6,14,15].

Limited work has been done on quantifying the effects of thermal history, microstructure and steel chemistry on martensite softening kinetics using rapid heat treatments consistent with those associated with laser welding [16–18]. These studies used a characteristic equation, such as the Johnson–Mehl–Avarmi–Kolmogorov (JMAK) equation [19–22], to characterize the softening kinetics. In these cases,

the softening kinetics were derived from a series of rapid isothermal tempering experiments designed to allow for the calculation of the tempering activation energy and rate exponent. Although these studies did show that transient softening could be quantified and predicted, the derived tempering activation energies and rate constants did not agree with those of the classic martensite tempering literature [16]. As it has been widely reported that martensite tempering is responsible for HAZ softening [6,7,9–11,13,15,16,23], it was expected that the activation energy for the softening process would be approximately 80–123 kJ/mol, the activation energy for C diffusion in ferrite [24,25], and the JMAK exponent would be approximately 0.67, the value associated with the precipitation of particles on dislocations [26]. Instead, the activation energy and rate exponent derived were approximately 28.3 kJ/mol and 0.10, respectively, for the martensitic M220 alloy [16]. Biro et al. [16] suggested that this disagreement was due to several processes being combined within the rapid tempering data, namely: martensite tempering, cementite precipitation and growth, ferrite recrystallization and grain growth. Unfortunately, without a clear understanding of the underlying processes responsible for HAZ softening, this process cannot be modeled or predicted phenomenologically. Thus, the current study will re-examine the data of Biro et al. [16] and expand the previous rapid tempering study for the fully martensitic M220 steel in order to more fully determine and decouple the metallurgical processes responsible for softening during rapid tempering as applied to HAZ softening in advanced steels.

2. Experimental methods

All experiments were carried out using an industrially fabricated 1.8 mm thick M220 grade martensitic steel. The as-received microstructure was produced via a continuous annealing line. The M220 chemical composition and as-received hardness can be found in Table 1. Microhardness traverses conducted on the sheet

cross-sections revealed that there were no significant hardness variations across the sheet thick thickness.

All rapid tempering heat treatments were carried out using a Gleeble 3500 (Dynamic Systems Inc., Poestenkill, NY, USA). Samples comprised 100 mm × 12 mm coupons with the rolling direction parallel to the sample long axis. During tempering, average sample heating and cooling rates were approximately 2200 °C/s and 4100 °C/s, respectively. These heating and cooling rates allowed the rapid tempering cycles to be considered isothermal, as verified via a Hollomon-Jaffe analysis [27] of the thermal profiles. Details of this analysis, with sample thermal profiles, are provided in Appendix A. Experimental tempering times and temperatures are listed in Table 2. However, it should be noted that tempering times of 20 s and 50 s were used only for tempering temperatures of 420 °C or less.

All microhardness measurements were made using a Vickers indenter on metallographically prepared sample cross sections. In all cases, a 500 gf load and 15 s dwell time were employed. Testing locations were separated by at least three indentation widths in accordance with ASTM E384-11 [28]. All microhardness data presented are the average of at least 10 measurements taken across the material thickness in order to account for any through-thickness heterogeneity. Error bars on the microhardness measurements represent the 95% confidence interval (CI) of the average microhardness value. In cases where data are presented without visible error bars, the 95% CI was smaller than the size of the plot symbol.

The microstructures of selected samples were examined using optical (OM) and scanning electron microscopy (SEM). In all cases samples were sectioned, mounted, and polished using standard metallographic methods. SEM samples were etched with 2% nital and gold coated before imaging with a JEOL JSM-6460LV SEM (JEOL Ltd., Tokyo, Japan) using an acceleration voltage of 20 keV. Optical microscopy samples were etched with Marshall's reagent. Grain size measurements utilized the linear intercept method [29].

All carbide equivalent diameters were measured from carbon replicas from samples tempered at either 500 °C or 600 °C viewed via transmission electron microscopy (TEM). Replicas were made using standard methods, as described in [6], and were observed using a Philips CM12 TEM (Royal Philips Electronics, Amsterdam, The Netherlands) at an acceleration voltage 120 keV. Carbides were identified manually and their equivalent circular diameter determined using Clemex Vision – Professional Edition ver. 5.0.008e (Longueuil, Quebec, Canada) image analysis software.

Table 1
Chemistry (in wt%) and hardness of M220 experimental steel.

C	Mn	P	S	Si	Cr	Mo	Base hardness (HV)	Min hardness (HV)
0.23	0.4	0.01	0.01	0.20	0.02	0.00	478.0	200.0

Table 2
Temperatures and times used for experimental rapid tempering heat treatments.

Temperatures	Times
360 °C, 380 °C, 400 °C, 420 °C, 500 °C, 600 °C, 650 °C	0.2 s, 0.5 s, 1 s, 2 s, 5 s, 10 s, 20 s, 50 s

In this case, the equivalent circular diameter is defined as the diameter of a circle with the equivalent area of the measured carbide. The carbide size distribution from each tempering cycle was fit to a log-normal distribution to determine the average carbide diameter and sample standard deviation. All carbide diameters presented here represent the log-normal mean diameter for a particular tempering cycle. A minimum of nine fields were viewed per sample, with the number of carbides analysed per sample ranging between 1200 and 2500.

3. Johnson–Mehl–Avrami–Kolmogorov softening kinetics model

From past work it has been shown that softening in DP and martensitic steels can be modeled using a sigmoidal curve starting at the as-received alloy hardness and transitioning to a minimum hardness as heat input, temperature or tempering time increase [12]. By applying a simple normalizing transformation to the hardness data, the softening progression, ϕ, can be determined via [6,16]

$$\phi = \frac{H_{BM} - H}{H_{BM} - H_\infty} \qquad (1)$$

where H_{BM} is the as-received (base material) alloy hardness, H is the instantaneous measured hardness and H_∞ is the minimum alloy hardness, defined as the hardness after a 1 h furnace heat treatment at 650 °C. From this definition, ϕ progresses from 0 in the as-received condition with no softening, to 1, where tempering has been completed. In this form, the softening kinetics may be modeled using the Johnson–Mehl–Avrami–Kolmogorov (JMAK) equation [19–22]:

$$\phi = 1 - \exp(-kt^n) \qquad (2)$$

where t is time, n the reaction rate exponent and k the energy barrier to softening as described by the Arrhenius equation:

$$k = k_0 \exp\left(-\frac{Q}{RT}\right) \qquad (3)$$

where Q is the activation energy for softening, R the universal gas constant, T is temperature and k_0 a fitting parameter. Although the JMAK equation was developed to describe the growth of a daughter phase within a parent phase, it has been found to be suitable for the modeling of softening data with some minor modification [16]. In the case of the M220 steel used in this study, the JMAK equation (Eq. (2)) was used successfully by the present authors to model isothermal tempering hardness data [16]. However, the JMAK kinetics derived by Biro et al. [16] were not able to accurately predict the low temperature (i.e. $T \le 400$ °C) data added to the data set (see Fig. 1).

4. Results

4.1. Tempering data analysis

Although the JMAK equation was used previously by the present authors to successfully model M220 softening data, two issues were identified with respect to its use in modeling HAZ softening. Firstly, the values derived for Q and n (Eqs. (3) and (2))
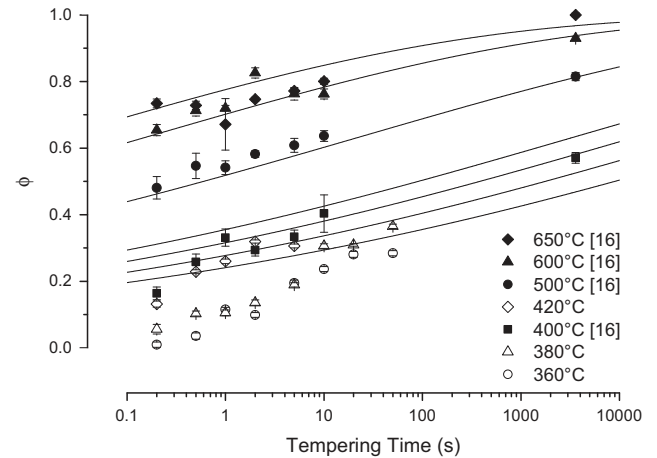
Fig. 1. Softening progress (ϕ) versus tempering time for experimental M220 alloy.

were 28.3 kJ/mol and 0.10, respectively [16]; values significantly lower than the established Q and n values of 80–123 kJ/mol [24] and 0.67 [26], respectively, determined for martensite tempering in the classic ferrous metallurgy literature. Secondly, the JMAK model was unable to adequately model the low temperature softening data. It was advanced that these discrepancies were due to multiple processes occurring during tempering [16].

In order to determine if multiple processes occurred during softening, which would affect the derived Q and n values [16] and accurate prediction of low temperature softening, the softening data were re-plotted as $\ln[-\ln(1-\phi)]$ versus $\ln(t)$ curves, as presented in Fig. 2. By transforming eq. (2) in this manner, n and k may be calculated directly from the slope and y-intercept of the $\ln[-\ln(1-\phi)]$ versus $\ln(t)$ plot, respectively. From Fig. 2, it can be seen that there are two distinct regions in the softening data, as characterized by the significant change in the slope of the 360–420 °C curves, suggesting that two distinct processes were operating for shorter and longer tempering times. These are referred to as Stage I and Stage II softening in Fig. 2 and in the subsequent discussion. A more detailed examination of Fig. 2 will reveal that the slopes of the Stage I portions of the curves are approximately parallel for all tempering temperatures as are the slopes of the curves for Stage II, indicating that similar processes are operating in each regime. In addition, the transition from Stage I to Stage II, as characterized by the time of the curve knee points, decreases significantly with increasing tempering temperature and was not able to be experimentally captured for temperatures higher than 420 °C. This latter is consistent with softening being a thermally driven process.

To determine the relationship between the two process regimes highlighted in Fig. 2 and the microstructural evolution of the samples as a function of tempering time, the microstructures of the as-received material and samples tempered at 400 °C and 500 °C were viewed via the SEM. The as-received base material comprised both non-tempered and tempered martensite grains, indicating that the as-received material had undergone some degree of autotempering during industrial thermal processing prior to welding (Fig. 3a). When tempered at 400 °C for times of 1 s or less, the microstructures were quite similar to those of the

base material, as can be seen in Fig. 3b and c. These observations, combined with the kinetic data from Fig. 2, imply that the martensite decomposition had not been completed for these microstructures and that the tempering reaction was on-going. In the classic tempering process sequence, this would correspond to Stage 3 of tempering [25]. At longer times and higher temperatures (Figs. 3c–g) the microstructures comprised tempered martensite with a significant population of carbides. These observations and the change in slope observed for the softening data in Fig. 2 suggest that carbide nucleation was complete and

that carbide coarsening or growth was underway. This corresponds to stage 4 of the classic tempering sequence [25]. The kinetics of each stage will be discussed separately in the below text.

4.2. Stage I softening – carbide nucleation from martensite

From the analysis of Fig. 2, it was determined that the average JMAK exponent (n) value for the 360–420 °C Stage I softening was 0.659 ± 0.003, which is in good agreement with the accepted literature value of 0.67 for particle nucleation on dislocations [26]. To determine the activation energy for Stage I softening, an Arrhenius plot (Fig. 4) was constructed using the k values derived from the 360 °C to 420 °C short-time tempering data in Fig. 2. From this construction, an activation energy, Q, of 113 ± 7 kJ/mol was calculated. This value is in good agreement with the activation energy for C diffusion in ferrite of 80–122 kJ/mol [24,25], which is widely accepted as the dominant process in the initial stages of martensite tempering.

It is interesting to note that the degree of softening (i.e. $\ln[-\ln(1-\phi)]$) value for the samples tempered at 360–420 °C was approximately -1.15 at the curve knee point in Fig. 2, corresponding to a ϕ value of 0.27 ± 0.05. Using a simple regression model, it may be calculated that for samples tempered at 500 °C, Stage I softening would be completed at approximately 0.06 s (see Table 3). Timescales of this order are extremely difficult to capture experimentally and explain the lack of a visible Stage I softening from the experiments with tempering temperatures greater than 420 °C (see Fig. 2).
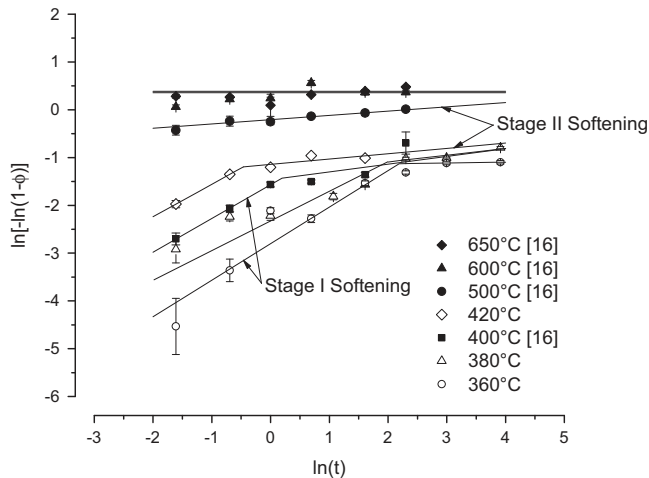

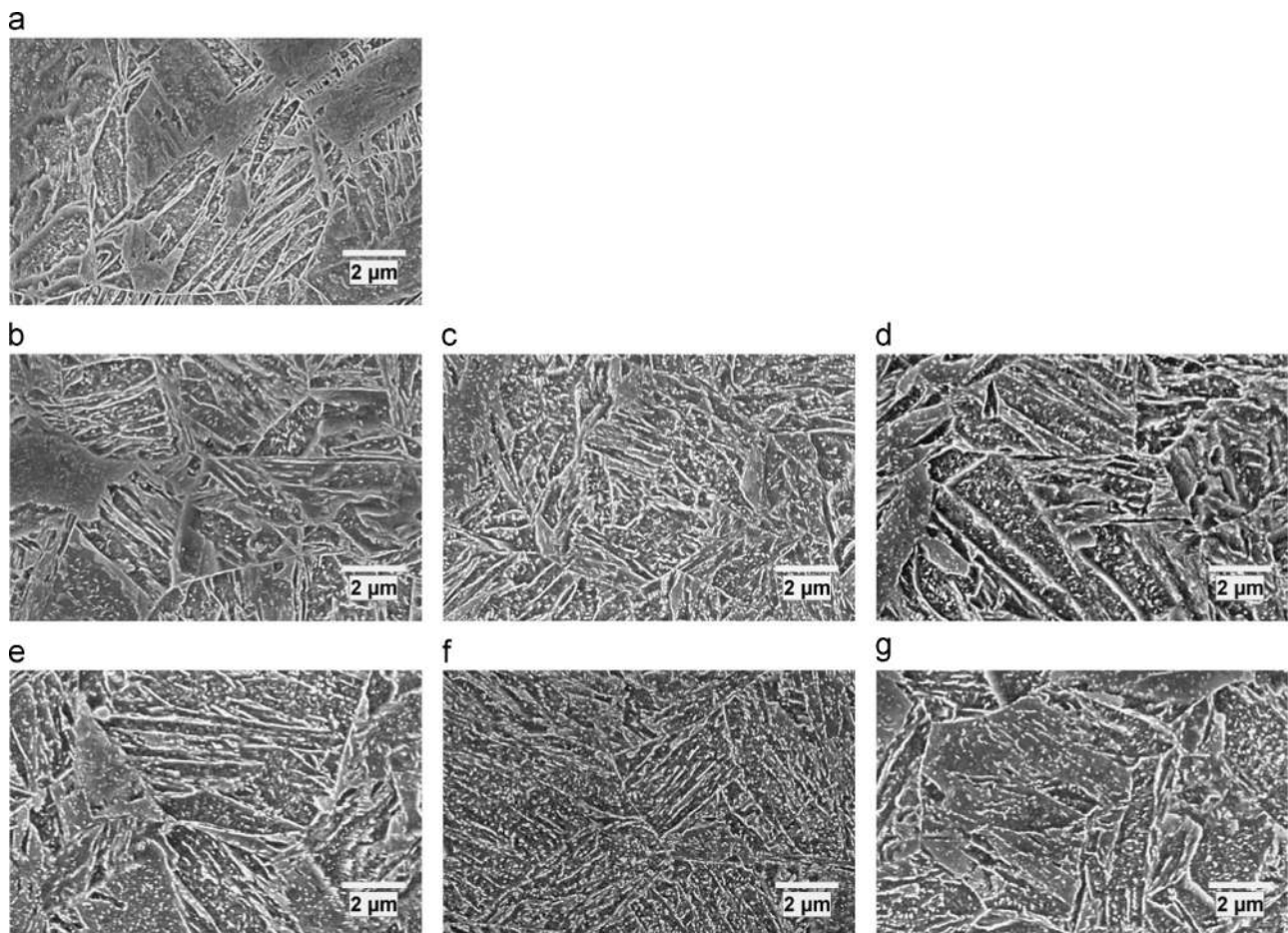**Fig. 2.** Logarithmic transformation of M220 softening data.

Fig. 3. SEM microstructures of the (a) as-received M220 and after tempering at 400 °C for (b) 0.2 s, (c) 1 s (d) 2 s and at 500 °C for (e) 0.2 s, (f) 1 s and (g) 2 s.
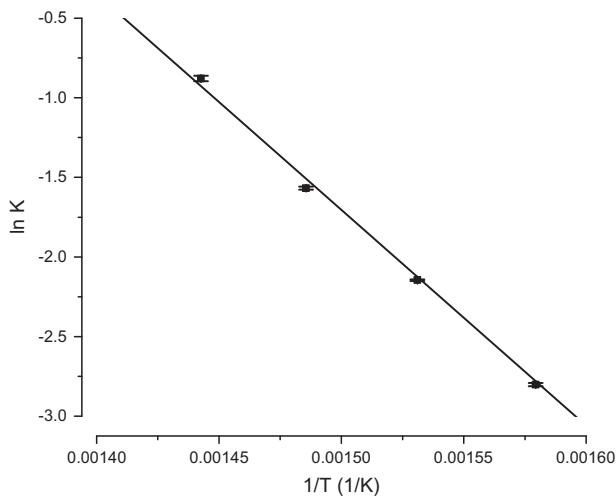
Fig. 4. Arrhenius plot of k versus $1/T$ for Stage I softening data (Fig. 2) for samples tempered between 360 and 420 °C.

Table 3
Time required to complete Stage I softening for tempering temperatures between 360 °C and 650 °C.

Temperature (°C)	Tempering time (s)
360	26
380	9
400	3.5
420	1.4
500	0.055
600	0.0023
650	0.0006

4.3. Ferrite grain size

After the carbide nucleation stage was completed, Fig. 1 through Fig. 3 show that the steel continued to soften through the martensite decomposition process. This could be due to a combination of three mechanisms: ferrite recrystallization, grain growth or softening associated with carbide growth. To investigate whether ferrite grain recrystallization or grain growth were significant factors in the softening process, a sample tempered at 500 °C for 0.2 s and a second sample tempered at 600 °C for 10 s were compared to determine if significant changes in the grain structure had occurred during the tempering heat treatments. These microstructures are presented in Fig. 5. Both samples exhibited a fine-grained, equiaxed microstructure where the average grain size for the samples tempered at 500 °C and 600 °C were 3.1 ± 0.1 μm and 2.5 ± 0.2 μm, respectively. The significantly smaller ferrite grain size of the sample tempered at 600 °C may be attributed to recrystallization, as reported by Speich [30]. However, it is believed that this slight reduction in grain size was not sufficient to have contributed significantly to the hardness changes observed in Fig. 1.

4.4. Stage II softening – carbide coarsening

From the above, it can be concluded that changes in the ferrite grain structure did not contribute significantly to Stage II softening (Fig. 2). From Fig. 3d–g and Fig. 5, it may be seen that these microstructures exhibited large populations of carbides. These carbides can block dislocation movement through a precipitation hardening mechanism [31], the effectiveness of which is a function of particle size and the inter-particle distance as described by the Ashby–Orowan equation [32].
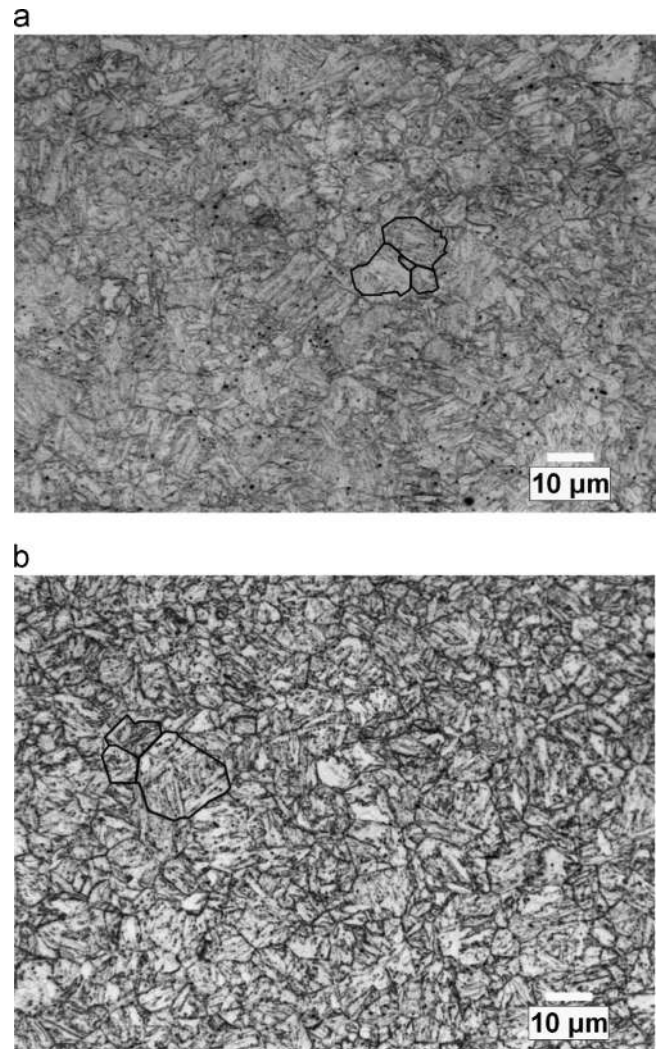

Fig. 5. Optical microstructures of samples tempered at (a) 500 °C for 0.2 s and 600 °C for 10 s. Examples of ferrite grains are outlined.

The carbides observed in the tempered M220 were identified as cementite for all TEM replicas examined [16]. Average equivalent cementite particle diameters were then plotted versus tempering time for the two temperatures (Fig. 6), from which it may be then seen that mean diameter of the cementite particles in samples tempered at 600 °C grew more rapidly than those tempered at 500 °C.

Cementite coarsening was consistent with the trends observed in the hardness data (Fig. 1), where particle size increased with increasing time and temperature, leading to a drop in precipitate density and decreased hardness. The contribution of carbide coarsening to the overall sample hardness can be calculated using a modified version of the Ashby–Orowan equation arising from Guo and Sha [32]:

$$\Delta H = 0.84 \frac{1.2 G b M_T}{2\pi q L} \ln \frac{d}{2b} \tag{4}$$

where ΔH is the change in hardness associated with precipitation hardening, G is the ferrite shear modulus (81 GPa, [32]), b is the Burgers vector (0.248 nm, [32]), M_T is the Taylor factor (2.75, [32]), q is the conversion factor between Vickers hardness and yield strength (2.9 MPa/HV [33]), d the carbide equivalent diameter and L the inter-particle spacing. The values of d and L were taken directly from the carbide size measurements and may be found in Table 4. The base hardness of the microstructure was assumed to be 92 HV from the hardness of ferrite plus contributions from solution strengthening alloying elements [34,35].
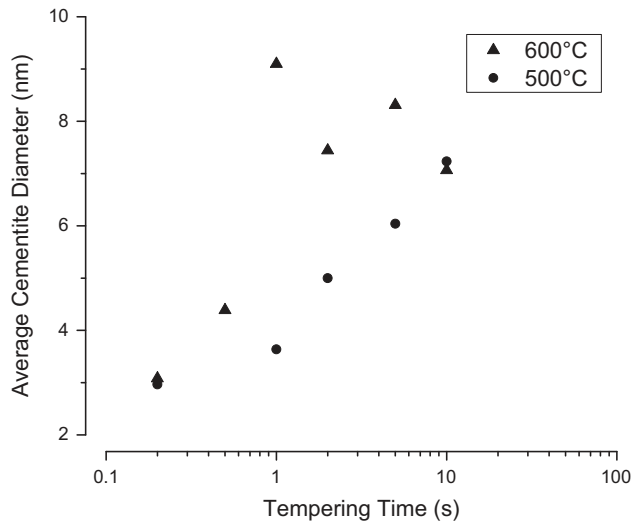
Fig. 6. Average carbide diameters measured from M220 samples tempered at 500 °C and 600 °C with tempering times between 0.2 and 10 s.

Table 4
Cementite equivalent diameter and densities with associated inter-particle distance and ΔH from samples tempered at 500 °C.

Tempering time (s)	Diameter (nm)	Particle density (nm^{-2})	Inter-particle distance (nm)	Calculated ΔH (HV)
0.2	2.97	1.72E-03	24.1	258
1	3.64	1.84E-03	23.3	309
2	5.00	6.13E-04	40.4	200
5	6.04	3.69E-04	52.0	166
10	7.23	3.68E-04	52.1	182

The influence of cementite particle size on hardness was calculated using Eq. (4) for samples tempered at 500 °C as the carbide size data for samples tempered at 600 °C was too noisy for a confident evaluation of its effect (Fig. 6). When the calculated hardness due to carbide coarsening was compared to the measured hardness values for samples tempered at 500 °C, it can be seen that predictions followed the softening trend reasonably well (Fig. 7). The average error from this prediction was 11%, which is reasonable considering the wide size distribution of the cementite particles measured. The agreement between the precipitation hardening model and the measured hardness values suggest that carbide coarsening dominated Stage II softening.

Although Stage II softening largely arises from interactions between the ferritic matrix and carbide coarsening during tempering, the kinetic parameters k and n may still be used to characterize the softening progression (Fig. 2). Using the analysis employed for Stage I softening, the average n value for carbide coarsening was determined to be 0.108 ± 0.001. Using the Stage II k data from Fig. 2 and the Arrhenius plot presented in Fig. 8, it was determined that the activation energy for the carbide growth process was 35 ± 4 kJ/mol. These values are in reasonable agreement with the values previously calculated for the entire softening process (28.3 kJ/mol and 0.10 [16]), which is not surprising as the majority of the data used to fit the JMAK parameters in [16] originated from the carbide coarsening stage.

5. Discussion

Decoupling the carbide nucleation and coarsening processes from the overall softening process revealed the reasons for the activation energy (Q) and JMAK exponent (n) of the combined softening processes in [16] not agreeing with the classic literature values for martensite tempering. As was shown in Fig. 2 through Fig. 4, when the
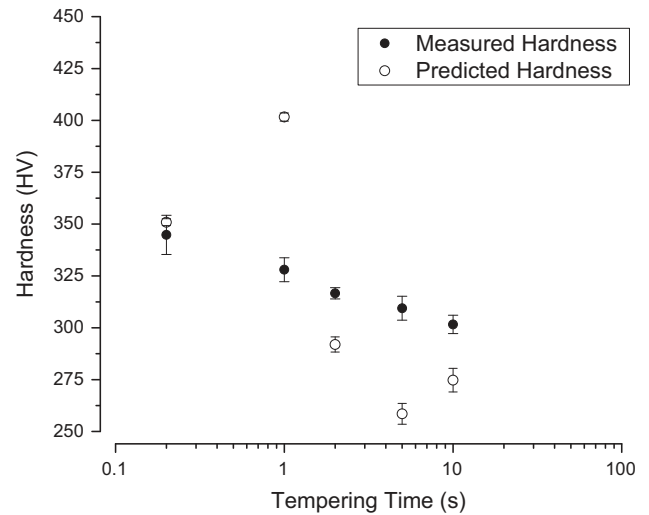

Fig. 7. Comparison between the measured hardness from samples tempered at 500 °C and the hardness predicted by the modified Ashby–Orowan model [32].
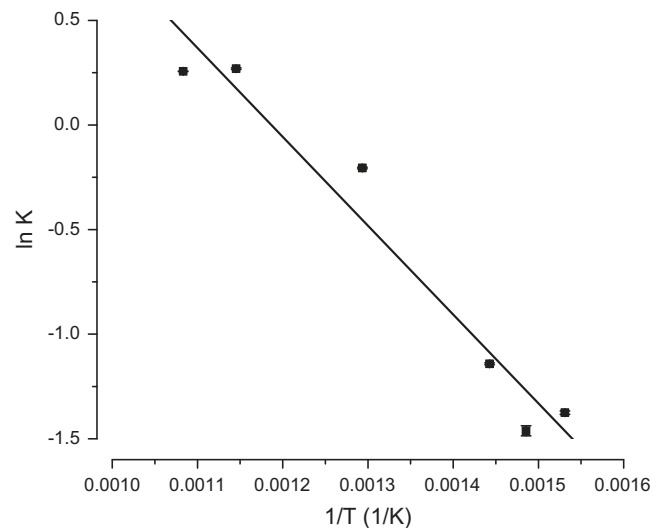

Fig. 8. Arrhenius plot of k versus $1/T$ for Stage II softening data (Fig. 2).

carbide nucleation process (Stage I in Fig. 2) was separated from the overall softening process, the calculated activation energy (113 kJ/mol) and JMAK exponent (0.67) agreed well with the classic literature values for martensite tempering. From this, it can be concluded that Stage I softening of the present martensitic steel can be characterized as being equivalent to stage 3 (i.e. nucleation of cementite) of the well-established martensite tempering process [25].

A similar procedure applied to the Stage II portion of the tempering data in Fig. 2 determined that the activation energy (Fig. 8) and JMAK exponent for the carbide growth process were 35 ± 4 kJ/mol and 0.108 ± 0.001, respectively. However, it must be acknowledged that an inspection of these values would seem to be at odds with the rate controlling processes for carbide growth, in this case the diffusion of C and self-diffusion of Fe. To resolve this seeming inconsistency, cementite growth kinetics need to be established.

5.1. Carbide growth during Stage II softening

Particle growth kinetics have been modeled by Lindsley and Marder [36] such that

$$d = k_D t^m \tag{5}$$

where d is the particle equivalent diameter, k_D is the diffusion dependent constant and m is the coarsening exponent, which depends on the dominant coarsening mechanism (i.e. $m=0.2$ for dislocation pipe diffusion, 0.25 for grain boundary diffusion and 0.33 for volumetric diffusion). By applying Eq. (5) to the particle growth data in Fig. 6, it was observed that the dominant diffusion mechanism changed between samples tempered at 500 °C and 600 °C. When tempering at 500 °C, m was found to be 0.25 ± 0.02, indicating that grain boundary diffusion was the dominant growth mode. However, at 600 °C, m was determined to be 0.29 ± 0.05, indicating that cementite growth was due to a combination of grain boundary and volumetric diffusion. The effects of these different diffusion mechanisms on the microstructural evolution of the tempered martensite may be seen in Fig. 9, where cementite within the samples tempered at 500 °C formed primarily on the martensite block and lath boundaries, whereas in the samples tempered at 600 °C, cementite grew on the lath and block boundaries as well as throughout the bulk grains. The observation that the cementite growth mechanism can change with tempering temperature is consistent with the results of Bannyh et al. [37], who also observed a progression from grain boundary to volumetric controlled diffusion when increasing the tempering temperature for a 0.83% C martensite. However, it should be noted that there is varied opinion in the literature on the mechanisms controlling cementite growth during martensite tempering. For example, Nam and Bae [38] found evidence of bulk, grain boundary, and dislocation pipe diffusion when analysing cementite growth of a 0.45% C martensite alloyed with Mn and Si after tempering at 700 °C. Similarly, Lindsley and Marder [36] found that cementite growth was controlled by a combination of grain boundary and pipe diffusion for various martensite chemistries with C contents ranging from 0.20–1.39% tempered at 690 °C. Conversely Das et al. [39] found that bulk diffusion was the sole mechanism responsible for cementite growth in Mn and Si-containing martensites with between 0.34% and 0.68% C tempered at 588 °C, 657 °C, and 680 °C. However, in spite of the disagreements on the operative mechanisms, the present results fit within the observations of other studies and are believed to be applicable for the present alloy chemistry and rapid tempering thermal cycles employed in this study.

As it was observed that cementite grew by both bulk and grain boundary control, the rate of each growth mechanism must be understood. Volumetric diffusion controlled particle coarsening kinetics have been described by Lifshitz and Slyozov per [40]

$$d^3 - d_0^3 = \frac{64\gamma D_V C_0 V_m}{9RT}(t - t_0) \tag{6}$$

where d is the particle diameter at time t, d_0 the particle diameter at time t_0, γ the surface free energy of the precipitate per unit area of precipitate-matrix interface, C_0 the equilibrium concentration of solute atoms in the matrix, V_m the molar volume of the precipitate and D_v the volumetric diffusion coefficient. Speight [41] described grain boundary diffusion controlled particle growth by

$$d^4 - d_0^4 = \frac{64\gamma D_{gb} C_0 V_m \delta}{3k_1 RT}(t - t_0) \tag{7}$$

where D_{gb} is the grain boundary diffusion coefficient, δ the grain boundary thickness and k_1 a geometric constant.

5.2. Correlation between activation energies of carbide growth and softening

As it was shown, above, that Stage II softening was due to cementite growth, it is logical to believe that the activation energy of softening is correlated to the activation energy for carbide growth. However, as the diffusion mechanism(s) controlling

particle growth changed with tempering temperature, the activation energy could not be calculated using a conventional Arrhenius plot. For this reason, literature values were used. Although cementite grows through diffusion of both C and Fe, the controlling process rate is the self-diffusion of Fe [42] because of its higher activation energy, where the activation energies for bulk and grain boundary self-diffusion of Fe are 234 kJ/mol [43] and 363 kJ/mol [44], respectively. Both of these activation energies far
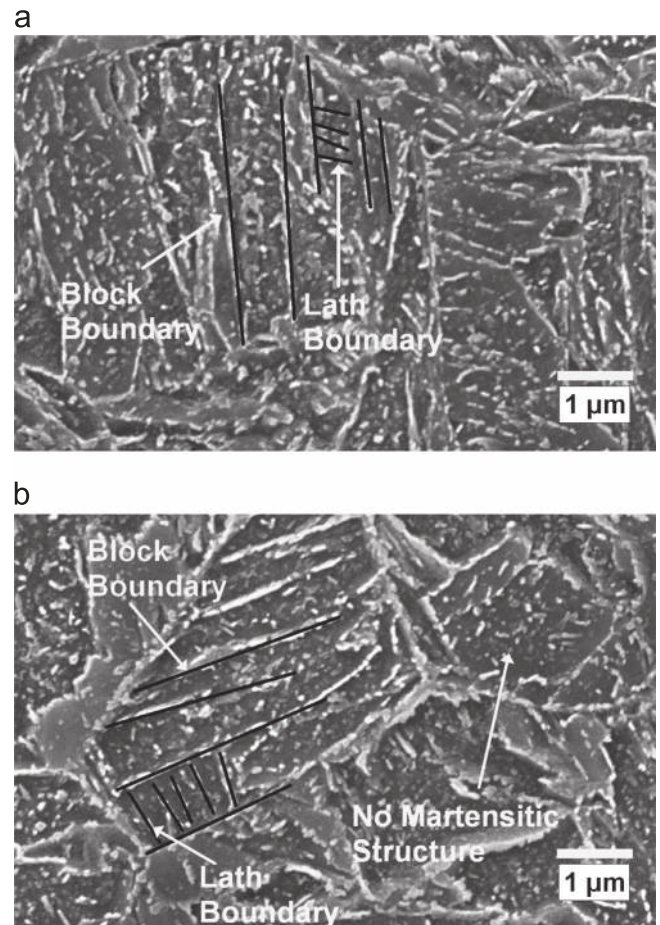

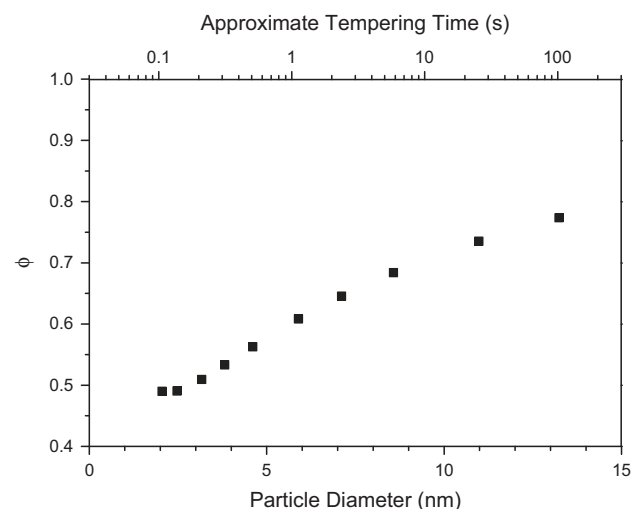Fig. 9. Martensite tempered at (a) 500 °C for 1 s and (b) 600 °C for 0.5 s.

Fig. 10. Softening progress (ϕ) versus cementite particle diameter for samples tempered at 500 °C.

exceed the measured activation energy of 35 ± 4 kJ/mol for Stage II softening. However, it must be remembered that the correlation between mean cementite diameter and softening (ϕ) is non-linear, which would have an effect on the apparent activation energy for the softening process.

To determine how the activation energies for Fe self-diffusion relate to the apparent activation energy for softening, it must first be understood how the softening progression (ϕ) varies with particle diameter (d). After determining how ϕ changes with d, correlating ϕ to time may be done through Eqs. (6) and (7) and the activation energy calculated per the methodology used in Sections 4.2 and 4.4. Since Eq. (4) relates hardness both to ln d and the reciprocal of L, both of which increase as d decreases, it was decided that a more direct way to correlate ϕ to d could be obtained by plotting ϕ versus d, as shown in Fig. 10. From this, it can be seen that ϕ increases as a power function of particle diameter such that

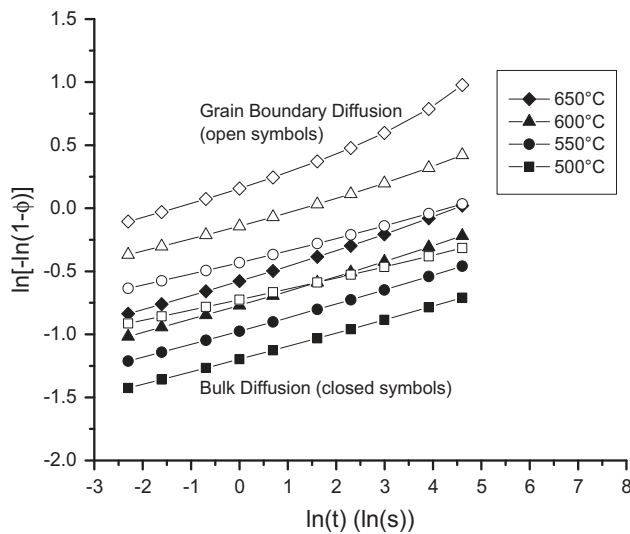$$\phi = 0.39 d^{0.26} \tag{8}$$

Fig. 11. Logarithmic transformation of softening resulting from calculated particle mean particle diameters assuming that growth is controlled by grain boundary diffusion alone or bulk diffusion alone.
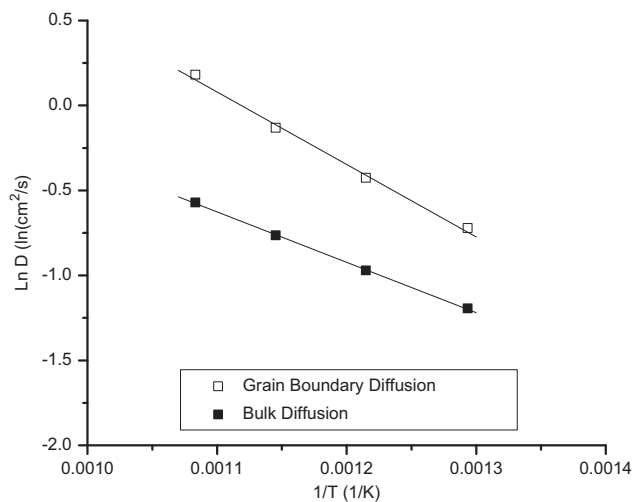

Fig. 12. Arrhenius plot of D versus $1/T$ for Stage II softening data resulted from particle growth calculated assuming either grain boundary or bulk diffusion driven growth (Fig. 11).

By substituting Eqs. (6) and (7) into d in Eq. (8), ϕ may be calculated as a function of time. For this calculation γ was taken to be 2.48×10^{-5} J/cm^2 [42], $V_m = 24$ cm^3/mol [45], $\delta = 5 \times 10^{-8}$ cm [44], and $k_1 = 5 \times 10^{-8}$ (which was chosen such that the mean cementite particle size matched the observed experimental values from this study). Both D_{gb} and D_V had Arrhenius forms where the activation energies, Q, matched the values listed above and the pre-exponential factors D_V^0 and D_{gb}^0 were 1.51 cm^2/s [43] and 6.97×10^5 cm^2/s [44], respectively. Calculating ϕ from cementite growth results in apparent activation energies for Stage II softening of 24 kJ/mol and 35 kJ/mol (see Fig. 11 and 12) when cementite growth is driven by bulk and grain boundary diffusion, respectively. These values match the measured activation energy for Stage II softening of 35 ± 4 kJ/mol determined in the present study. When it is considered that the dominant diffusion mode was grain boundary diffusion, the low activation energy determined for Stage II softening was likely due to the non-linear relationship between d and ϕ.

5.3. Correlation between rate constants of carbide growth and softening

As with the correlation between the activation energies associated with cementite growth and softening, the correlation between the JMAK exponent, n (Eq. (2)), and the time exponent for particle coarsening, m (Eq. (5)) is not clear. To determine this relationship, it is best to simplify the relation between ϕ and d using Eq. (8). By substituting the appropriate form of d from Eq. (5) for the 500 °C and 600 °C particle data into Eq. (8), the time exponent for ϕ would be 0.065 for the samples tempered at 500 °C and 0.075 for the 600 °C samples. However, in case of the JMAK equation (Eq. (2)), time is an exponential variable and is not easily isolated analytically. Thus, Eqs. (2) and (8) were equated and n determined using non-linear regression. This technique yielded a JMAK equation n value of 0.112 ± 0.001. This agrees well with the value of the JMAK exponent calculated from the hardness data during carbide coarsening (i.e. 0.108 ± 0.001) and shows how the non-linear relation between ϕ and d as well as the exponential form of the JMAK equation changes the rate constants from those expected from Eq. (5).

5.4. Applying the phenomenological model to softening predictions during rapid tempering

The overall conclusion of this study is that decoupling the short-time/lower temperature (i.e. Stage I, Fig. 2) carbide nucleation process from the longer-time/higher temperature carbide coarsening process (i.e. Stage II, Fig. 2) allowed for the derivation of JMAK parameters for rapid martensite tempering consistent with the existing classic literature C-diffusion controlled models for martensite tempering. However, in most practical cases of rapid high temperature tempering, such as weld heat affected zone softening, the softening process can be efficiently modeled using kinetic parameters derived from the coupled process due to the dominant role carbide coarsening plays in this processes. However, it should be noted that in cases where rapid tempering takes place at low temperatures (i.e. $T \leq 400$ °C) for short times, the carbide nucleation stage must be taken into account in the softening model because this will occur over a significant portion of the tempering cycle when tempering on the order of seconds or tens of seconds. This explains the poor fit between the predicted and actual ϕ values for the softening data in Fig. 1 for tempering temperatures of 400 °C or lower.
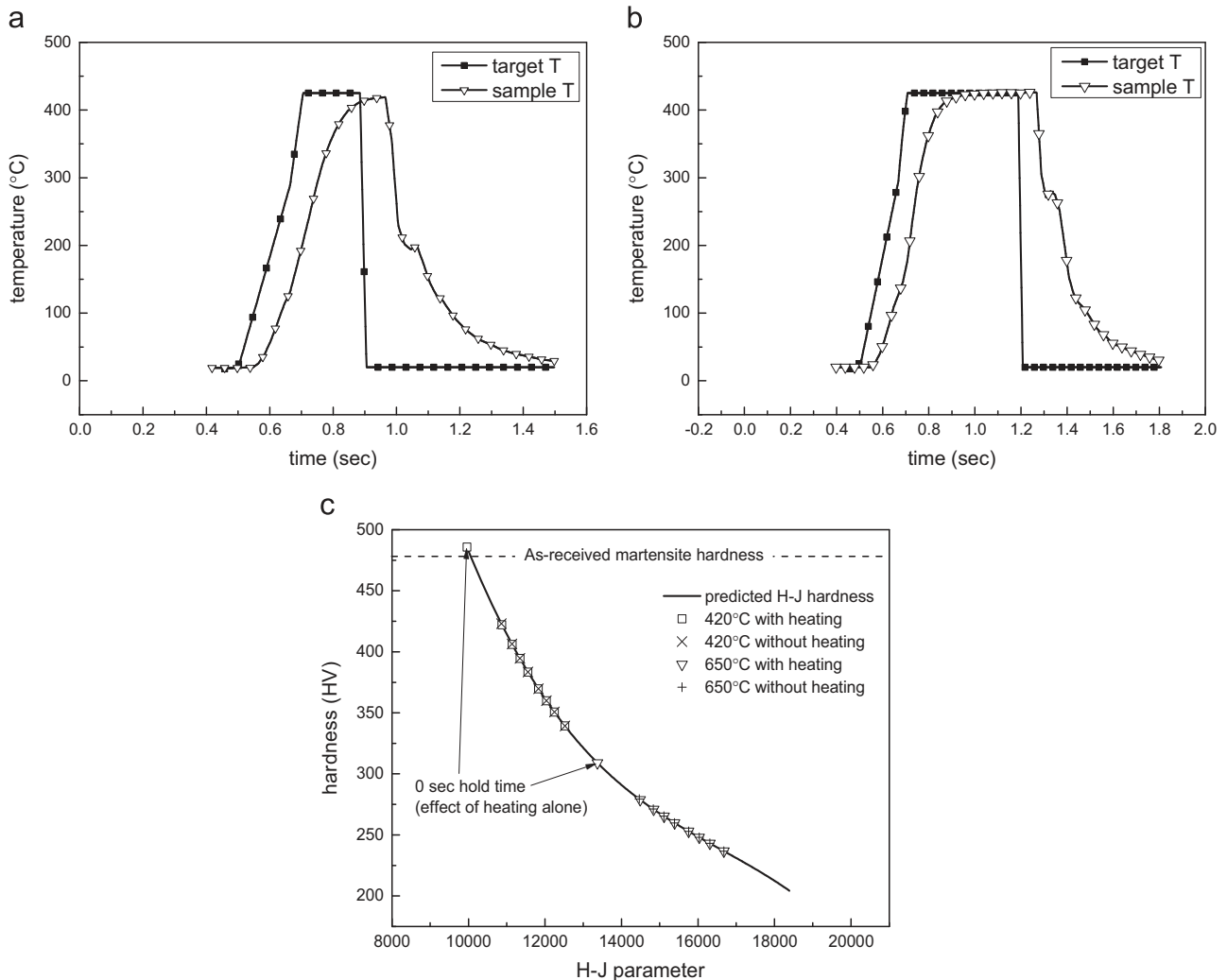
Fig. 13. Sample rapid tempering thermal profiles: (a) rapid tempering thermal cycle for 0.2 s at 450 °C; (b) rapid tempering cycle for 0.5 s at 450 °C; (c) results of Hollomon-Jaffe analysis of tempering damage for isothermal thermal cycles versus heating plus isothermal holding cycles at 420 °C and 650 °C.

6. Conclusions

This study examined the softening observed in a martensitic M220 steel during rapid tempering to resolve the disagreement between the activation energy and time exponent calculated by Biro et al. [16] with the widely accepted classic C-diffusion controlled mechanism of martensite tempering. It was found that:

1. The softening process could be broken down into two sub-processes: carbide nucleation and carbide coarsening. These processes were separated within the overall softening data by transforming the softening versus time data.
2. The carbide nucleation stage occurred very quickly and was experimentally observed only for relatively short tempering times and for tempering temperatures of less than 420 °C. The activation energy and time exponent for carbide nucleation, calculated from the hardness data, were determined to be 113 ± 7 kJ/mol and 0.659 ± 0.003, respectively, matching the classic literature values for the activation energy for C diffusion in ferrite (80–120 kJ/mol) and particle growth on dislocations (0.67) widely accepted for martensite tempering.
3. The apparent activation energy and time exponent calculated for the carbide coarsening stage of softening were 35 ± 4 kJ/mol and 0.108 ± 0.001, respectively. These values did not match

the classic literature values for the activation energy and time constant of 234 kJ/mol and 0.33 or 363 kJ/mol and 0.25 when cementite growth is dominated by volumetric and grain boundary diffusion, respectively.
4. The apparent activation energy associated with the carbide coarsening stage was determined to be an artefact of the non-linear relationship between the particle diameter growth kinetics and the self-diffusion of Fe, which is the controlling mechanism for cementite growth. When the apparent activation energy of Stage II softening was calculated using the softening resulting from cementite growth due to grain boundary and bulk diffusion, the resulting activation energy matched the activation energy calculated from experimental data.
5. The low time exponent associated with the carbide coarsening stage was due to the non-linear relation between the softening parameter (ϕ), cementite particle diameter and the exponential form of the JMAK equation.
6. Although this work revealed that there are two separate processes occurring when softening during rapid tempering, it is believed that in most cases softening during rapid tempering may be modeled using a kinetic model dominated by the carbide coarsening process as this process dominates at practical timescales and higher welding heat inputs. However,

in the case of short-time tempering at temperatures of 400 °C or less, the carbide nucleation stage must be taken into account in order to predict softening.

Acknowledgements

Appendix A. Verification of use of isothermal tempering assumption

The use of the isothermal tempering assumption in the modeling was verified via a Hollomon-Jaffe [27] analysis of the tempering damage arising from rapid tempering cycles. Examples of typical short isothermal hold time thermal cycles employed in the Gleeble simulations – 450 °C for 0.2 s and 450 °C for 0.5 s – are shown in Fig. 13(a,b), respectively.

The relative contributions of the heating versus isothermal portion of the Gleeble simulation thermal cycles (Fig. 13(a,b)) on tempering damage was determined by calculating the tempered hardness of the material after tempering at 420 °C and 650 °C using two models for the thermal cycle: (i) a thermal cycle that comprised only the isothermal tempering temperature and time – i.e. a rectangular thermal profile and (ii) a thermal cycle comprising the heating portion of the cycle and the isothermal tempering temperature and time. Isothermal tempering times for the 420 °C and 650 °C data ranged from 0 s. (i.e. heating only without an isothermal hold) to 50 s. The effect of heating time on tempering damage was accounted for using the temperature domain method [18], where an equivalent isothermal tempering time at the peak tempering temperature arising from the heating portion of the tempering thermal profile was determined and added to the actual isothermal holding time at the peak tempering temperature. The tempered hardness was calculated using the experimental hardness data presented in Fig. 1 and Hollomon–Jaffe tempering parameter [27]. The results of this analysis are presented in Fig. 13(c). To simplify the presentation of these calculations, the predicted isothermal tempered hardness was approximated by a third-order polynomial fit ($R^2 = 0.975$). By overlaying the predicted hardness values of the tempering cycles accounting for and discounting the heating portion of the thermal cycles (Fig. 13(c)), it can be seen that there was no significant effect of excluding the heating portion of the cycle on the hardness, thereby validating the isothermal tempering assumption in the present analysis.

References

[1] U.S. Government, Federal Register 74, 2009, pp. 49454-49789.
[2] W. Gan, S.S. Babu, N. Kapustraka, R.H. Wagoner, Metall. Mater. Trans. A 37A (2006) 3221–3231.
[3] R.G. Davies, Metall. Trans. A 9A (1978) 671–679.
[4] B.C. De Cooman, Curr. Opin. Solid State Mater. Sci. 8 (2004) 285–303.
[5] K. Kunishige, Y. Nobuyuki, T. Taka, T. Nagao, SAE Tech. Pap. Ser. (1983) 830632.
[6] E. Biro, J.R. McDermid, J.D. Embury, Y. Zhou, Metall. Mater. Trans. A 41A (2010) 2348–2356.
[7] S. Hashimoto, S. Kanbe, S. Masatoshi, Trans. Iron Steel Inst. Jpn. 21 (1981) B-497.
[8] N. Yamauchi, T. Taka, K. Kunishige, N. Nagao, Trans. Iron Steel Inst. Jpn. 22 (1982) B-107.
[9] P.K. Ghosh, ISIJ Int. 30 (1990) 317–324.
[10] P.K. Ghosh, P.C. Gupta, Ramavtar, B.K. Jha, Weld. J. 70 (1991) 7s–14s, http://aws.org/wj/supplement/WJ_1991_01_s7.pdf.
[11] P.K. Ghosh, P.C. Gupta, O.M. Pal, R. Avtar, B.K. Jha, V. Sagar Dwivedi, ISIJ Int. 7 (1993) 807–815.
[12] M. Xia, E. Biro, Z. Tian, Y.N. Zhou, ISIJ Int. 48 (2008) 809–814.
[13] V.H. Baltazar Hernandez, S.K. Panda, M.L. Kuntz, Y. Zhou, Mater. Lett. 64 (2010) 207–210.
[14] E. Biro, A. Lee, Welded properties of various DP600 Chemistries, in: Sheet Metal Welding Conference XI, 2004, paper 5-2.
[15] S.S. Nayak, V.H. Hernandez Baltazar, Y. Zhou, Metall. Mater. Trans. A 42A (2011) 3242–3248.
[16] E. Biro, S. Vignier, C. Kaczynski, J.R. McDermid, E. Lucas, J.D. Embury, Y.N. Zhou, ISIJ Int. 53 (2013) 110–118.
[17] S. Vignier, E. Biro, M. Hervé, Weld. World 58 (2014) 297–305.
[18] J. Shi, C.R. Liu, Trans. ASME 127 (2005) 476–483.
[19] W.A. Johnson, R.F. Mehl, Trans. Am. Inst. Miner. Metall. Eng. 135 (1939) 416–458.
[20] M. Avrami, J. Chem. Phys. 7 (1939) 1103–1112.
[21] M. Avrami, J. Chem. Phys. 8 (1940) 212–224.
[22] M. Avrami, J. Chem. Phys. 9 (1941) 177–184.
[23] V.H. Baltazar Hernandez, S.S. Nayak, Y. Zhou Metall., Mater. Trans. A 42A (2011) 3115–3129.
[24] J.F. Shackelford, W. Alexander, CRC Materials Science and Engineering Handbook, Third ed., CRC Press, Boca Raton, 2001.
[25] R.W.K. Honeycombe, H.K.D.H. Bhadeshia, Steels: Microstructure and Properties, second ed., Butterworth-Heinemann, Oxford, 1995.
[26] J.W. Christian, Theory of Transformations in Metals and Alloys, Part 1, second ed., Pergamon Press, Oxford, 1975.
[27] J.H. Hollomon, L.D. Jaffe, Trans. Am. Inst. Miner. Metall. Eng 162 (1945) 223–248.
[28] ASTM E-384-11e1, Standard Test Method for Knoop and Vickers Hardness of Materials, ASTM International, West Conshohocken, 2011.
[29] ASTM E112-12, Standard Test Methods for Determining Average Grain Size, ASTM International, West Conshohocken, 2012.
[30] G.R. Speich, Trans. Met. Soc. AIME 245 (1969) 2553–2564.
[31] W.R. Tyson, Acta Metall. 11 (1963) 61–62.
[32] Z. Guo, W. Sha., Mater. Sci. Technol. 18 (2002) 529–533.
[33] J.R. Cahoon, W.H. Broughton, A.R. Kutzak, Metall. Trans. 2 (1971) 1979–1983.
[34] E.C. Bain, Functions of the Alloying Elements in Steel, American Society of Metals, Cleveland, 1939.
[35] W.C. Leslie, Metall. Trans. 3 (1972) 5–26.
[36] B.A. Lindsley, A.R. Marder, Acta Mater. 46 (1998) 341–351.
[37] O. Bannyh, H. Modin, S. Modin, Jernkont. Ann. 142 (1962) 774–806.
[38] W.J. Nam, C.M. Bae, Scr. Mater. 41 (1999) 313–318.
[39] S.K. Das, A. Biswas, R.N. Ghosh, Acta Metall. Mater. 41 (1993) 777–781.
[40] I.M. Lifshitz, V.V. Slyozov, J. Phys. Chem. Solids 19 (1961) 35–50.
[41] M.V. Speight, Acta Meta. 16 (1968) 133–135.
[42] P. Deb, M.C. Chaturvedi, Metallography 15 (1982) 341–354.
[43] R.J. Borg, D.Y.F. Lai, J. Appl. Phys. 41 (1970) 5193–5200.
[44] E. Budke, Ch. Herzig, H. Wever, Phys. Status Solidi A 127 (1991) 87–101.
[45] S. Björklund, L.F. Donaghey, M. Hillert, Acta Metall. 20 (1972) 867–874.